3D pore analysis of gasoline particulate filters using x-ray tomography: Impact of coating and ash-loading

Heeje Seong[1], Seungmok Choi[1], Katarzyna E. Matusik[2], Alan L. Kastengren[2] and Christopher F. Powell[1]*

[1] Center for Transportation Research, Argonne National Laboratory, 9700 South Cass Avenue, Argonne, Illinois 60439, U.S.A.

[2] X-Ray Science Division, Argonne National Laboratory, 9700 South Cass Avenue, Argonne, Illinois 60439, U.S.A.

*Corresponding author. Tel: +1 630 252-9239. E-mail: hseong@anl.gov (Hee Je Seong) Smchoi81@gmail.com (S. Choi), kmatusik@anl.gov (K. Matusik), akastengren@anl.gov (A. Kastengren), powell@anl.gov (C. Powell)

Keywords: gasoline particulate filter (GPF); pore structure; X-ray tomography; ash; aging

Abstract

Since particulate emissions control technologies are dependent on filtration technologies, development of porous materials with optimized pore structures is crucial to improve filtration efficiency and pressure drop across filters. Despite increasing attention to 3D measurements of porous materials, however, there are few reports of pore structure investigations of diesel/gasoline particulate filters (D/GPFs) using 3D visualization techniques. In this work, GPF 3D pore structures were examined using x-ray tomography (XRT) to identify the impacts of catalyst coating or ash-loading. Voxel resolution of 2.93 μm made it impossible to distinguish coating or ash materials from the cordierite substrate, or to recognize smaller pores than the voxel resolution. However, pores up to 200 μm, which are responsible for most pore volume, were successfully analyzed. Coating and ash-loading resulted in lowering average pore diameter, total porosity, and open porosity, as the peak density of pore diameter at 60 μm decreased while pores below 20 μm increased. Also, the visualized closed pores, which were homogeneously distributed throughout the bare filter, tended to get larger from inlet to outlet sides and more likely to be on the surface inlet due to coating and ash-loading, indicating gas pathways originally existing in open pores were blocked due to coating and ash-loading, leading to increased pressure drop. The ash impact was found to be more noticeable on mid and back positions than on front position. In addition, the investigation of areal porosity along the direction of gas flow suggested that while ash penetration could reach the outlet side as noted from increased closed pore population, most ash particles would be contained up to 150 μm. The 2D cross-cut microscopic analysis that requires destructive procedures with the limited examination area could provide underestimation of ash penetration, whereas the 3D XRT

analysis seems to provide more accurate information of pore structure changes due to ash loading at different locations.

1. Introduction

Due to the hazardous impacts of particulate emissions on human health, filtration technologies have been applied to diesel and gasoline engines to trap and oxidize particles on porous cordierite, SiC and metal foam filters. Combustible carbon particles or soots are removed from filters during the regeneration process, but unwanted inorganic compounds originating from engine oil additives, fuel additives and engine wear gradually accumulate and block pores in filters, resulting in adverse effects on fuel efficiency from increased pressure drop [1]. Therefore, there have been on-going efforts to optimize filter designs considering catalyst coating, ash-derived long-term filtration efficiency and pressure drop as well as initial soot-laden performance [2, 3].

Ash impacts on filter performance have been intensively examined for diesel particulate filters (DPFs) [1], while more recent research has included gasoline particulate filters (GPFs) [4–6]. Visual observations of ash-loaded filters, which were performed by measuring thickness with sectioned parts or 3D computed tomography, indicated that ash deposits are significant on channel walls as well as on the back side as ash plugs [1, 6, 7]. High-resolution 3D tomography of an ash-loaded filter showed that surface pores were filled with ash [4]. Therefore, it is understood that soot containing ash first filled surface pores, then oxidized during the regeneration process, resulting in ash accumulation and plugging of pores from repeated soot oxidation. As a result, ash accumulates on channel walls up to a certain point and additional ash finds somewhere in the back side during continued soot oxidation and ash accumulation processes [1].

Since real-time particle filtration process is not observable in real world, simulating gas-particle flow and particle trap has been developed to better understand complex filtration process in pore levels of filters. The pore-scale flow analysis with the Brownian dynamics method showed that dominant filtration mechanisms of smaller and larger particles are ascribed to the Brownian diffusion and direct interception, respectively [8, 9]. Although detailed filtration trends would be different depending on the models that consider median pore sizes, deposit density, permeability, flow rate and other parameters, these numerical and simulating tools are found to be quite accurate at predicting filtration efficiencies and pressure drops despite assumed parameters. While most modeling works have been focused on DPFs, there have been a few modeling studies performed with GPFs. Recent studies with a heterogeneous multiscale filtration (HMF) model considering a pore size probability density function (PDF) and an inhomogeneous porosity distribution revealed that the dynamic particulate filtration process in GPFs were accurately predicted by comparing with experimental data [10, 11]

Mercury intrusion porosimetry (MIP) has often been used for measurements of pore sizes in materials. However, the method is known to underestimate or overestimate pore sizes as high intrusion pressure can damage and distort pore structures, while estimates of the interfacial surface tension and contact angle limit the accuracy of the measurements [12, 13]. Accordingly, direct porosity analysis using visualization methods has gotten increasing attention for filter applications, as digitized reconstructed images can be further integrated into mathematical simulations for predicting gas and fluid transport in porous filters [14–16]. X-ray tomography (XRT), scanning electron microscopy (SEM) and focused ion beam (FIB) SEM are often used to visualize 3D porous materials in many other applications [17–22], though their accuracy is limited by image resolution.

Pore analysis performed by 3D XRT provides useful information for DPF/GPF studies as detailed measurements of pore structures can help understand and predict pressure drop and flow patterns through porous walls using simulation. Despite advancement in this technology, however, there are few reports on the effects of catalyst coating and ash-loading on pore structure, including pore size, porosity and closed/open pores. In this work, we investigated 2D and 3D images of GPF single-channel walls obtained from the synchrotron XRT analysis to better understand how the catalyst coating and ash-loading impacted detailed pore structures of GPFs from inlet to outlet positions. The visualization and quantified results clearly indicated great impacts of ash loading on filter wall from inlet to outlet sides, rather than surface-level inlet as known from the 2D cross-cut microscopic analysis.

2. Experimental Procedure

2.1 Engine, GPF test setup and TWC information

A 2.4 L 4-cylinder, naturally aspirated, GDI spark-ignition engine was used to generate ash loading in the GPFs studied in this work. The engine was mounted on a 112 kW blower-cooled AC dynamometer for speed control and torque measurements. A three-way catalyst (TWC)-coated GPF (2 inch in diameter and 6 inch in length) was installed in a partial flow bench-scale reactor for ash loading. A bare GPF has 200 cells/in^2 and a wall thickness of 0.012 in (200/12) with 65% porosity from an MIP measurement and the TWC coating level was 50 g/L. For accelerated ash loading, commercially available engine lubricating oil (ILSAC GF-5 conventional motor oil, API SN rated, SAE grade 5W-20) was dosed into the fuel supply line to achieve 2 wt. % of the lubricating oil in gasoline fuel under space velocity of 40,000 h^{-1}, which allows about 1 g/L of ash loading per hour at 1250 rpm – 25% (The unit of g/L is the amount of ash loaded in the 1 L volume of a filter). The inlet gas temperature of the filter was maintained at approximately 350 °C during the oil doping step. To oxidize the collected soot and engine oil, an air heater was used to intermittently increase the GPF inlet temperature to 550 °C. More detail is found in Shao et al. [5].

The pressure drop and temperatures across the filter were measured, and the particulate number and mass filtration efficiencies were calculated by measuring total particulate numbers and soot mass upstream and downstream of the filter. Soot mass concentration was measured using a photo-acoustic sensor (AVL 483 micro soot sensor), and particulate number and size distribution were measured in the range of 17 to 600 nm using a scanning mobility particle sizer (SMPS, TSI Model 3936) with a condensed particle counter (CPC, TSI Model 3022A), coupled with a dilution tunnel (Dekati FPS-4000). The temperatures of the sampling probe and primary dilution air used in the dilution tunnel were controlled at 350 ^{o}C to remove condensed particles. The actual dilution ratios were calculated in the range of 120 to 150 from measuring the CO_2 concentrations before and after dilutions using an infrared CO_2 analyzer (California Analytical Instrument, Inc., Model 200).

2.2 XRT measurements

X-ray tomography measurements were performed at the 7-BM beamline of the APS [23]. Figure 1 schematizes the experimental setup. Further information with regard to the general setup and data acquisition pipeline may be found in previous work [24]. There are three filters prepared for the measurements: a bare filter, TWC-coated filter and 20 g/L ash-loaded filter. For the ash-loaded filter, small pieces of samples (4 mm x 4 mm, 4 cells) were taken from front, middle and back sides of the filter. In brief, each particulate filter was individually mounted on an air-bearing rotary stage. A 4 mm x 6 mm (V x H) polychromatic x-ray beam first passed through two metal foils that filtered low-energy x-rays in order to minimize heat load on the sample. The beam then impinged on the particulate filter, which absorbed a fraction of the incident x-ray photons, creating varying levels of contrast across the beam cross-section depending on the filter's thickness and material composition. Downstream of the rotation stage, photons that transmitted through the filter were partially absorbed by a 100 µm-thick cerium-doped lutetium aluminum garnet (LuAG:Ce) scintillator, which fluoresced due to the incident x-rays, creating a projection image of the sample. The resulting image was magnified with a 2x objective lens and recorded with a CMOS camera. Each particulate filter was rotated from 0° to 360°, with images recorded every 0.1°. The 2x objective lens provided an effective pixel size of 2.93 µm. In order to increase the signal-to-noise ratio, five images were recorded and subsequently averaged at each measured angle. The image stack was reconstructed using TomoPy, an open-source Python algorithm for synchrotron tomography [25].

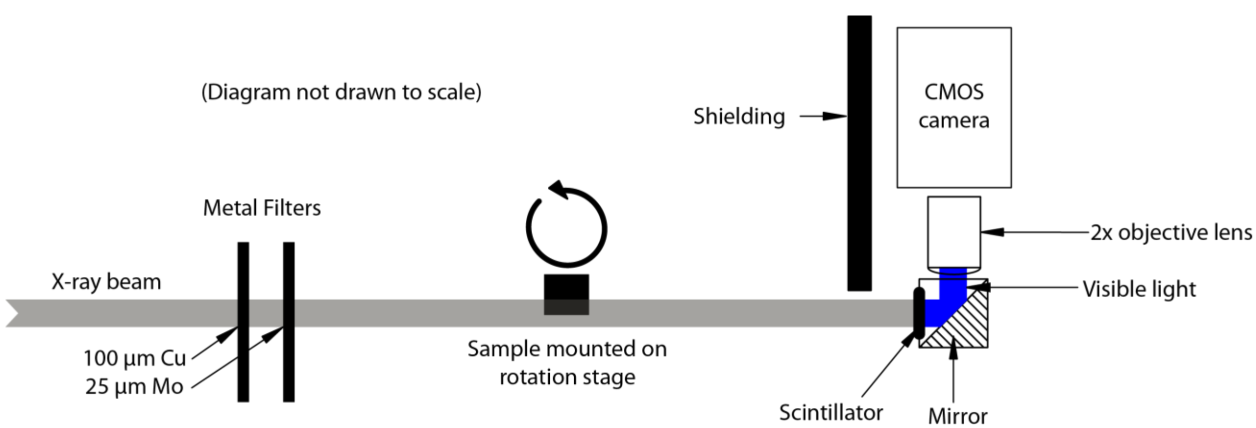

Fig. 1. Schematic of the experimental setup as viewed from above. The polychromatic x-ray beam from the synchrotron source is traveling from left to right.

2.3 Image processing

Avizo 9.0 (Thermo Fisher Scientific) was used to reconstruct 3D images and analyze pore information. Fig. 2 shows the image processing procedure from original raw sample image to 3D labeled image.

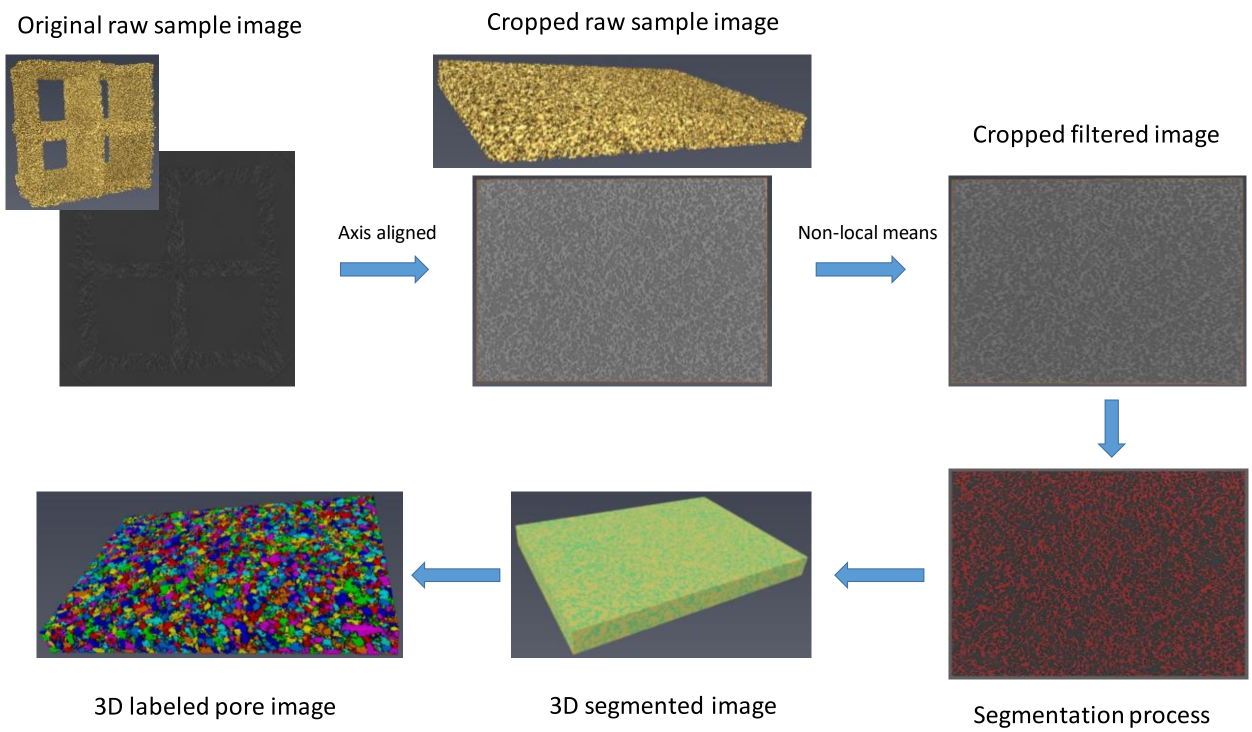

Fig. 2. Image processing procedure of XRT images using Avizo software.

a. Sample alignment and wall selection

Three different single-channeled walls were selected for each sample to statistically evaluate pore structures. Since each sample was not well aligned with any coordinate axis, it was aligned to a certain axis from a flat wall surface using the Isosurface function.

Then, each wall was sliced and the cropped image was obtained using the command of Resample Transformed Image.

b. Filtered image

Image filtering was used to reduce noises or artifacts and enhance edges between pores and materials. For this work, the Non-Local Means Filter was employed in this work, which was effective at reducing noises significantly while preserving edges.

c. Segmentation and pore/material assignment

The segmentation was performed to separate pore from material. Since the color contrast/resolution was not sufficient enough to isolate the filter material from ash, the material include the filter material and ash. The threshold of the magic wand function was carefully adjusted, monitoring 2D images of xy, xz and yz, and the optimized threshold was applied to the entire slices for 3D images. Then, the Arithmetic function was used to assign pores.

d. Separate objects and labeling

The Separate Objects function uses the Chamfer-Conservative method to cut pores, which performs the job from a combination of watershed, distance transform and numerical reconstruction algorithms. The neighborhood that refers to the type of connectivity for processing adjacent voxels was set at 26 among 6, 18 and 26, and the marker extent that specifies a number as a contrast factor was set at 1 for the entire images. With lower neighborhood and higher marker extent values, pore sizes tend to be smaller and the size distribution was inconsistent for each sample, which is assumed to be due to wrong recognition of pore connections. Then, the labeling was performed to convert the binary image of separated pores to a label image. The neighborhood value was set at 26 for the entire images.

e. Label analysis

Areas and volumes of 3D pores were calculated and the pore diameters were computed from volumes assuming spherical particles as follows;

$$Pore\ diameter = \sqrt[3]{\frac{6 \cdot Volume}{\pi}} \qquad \text{Equation 2.1}$$

f. Other computation

The Centroid Path Tortuosity module was used to compute tortuosity of a path by the centroids on each plane along the z-axis, from the ratio between the length of the path and the plane distance. Open pores are defined as connected pores, and the remaining pores are thereafter recognized as closed pores by the sieve analysis. Accordingly, the open porosity and closed porosity are calculated. Areal porosity from inlet to outlet was computed from 2D labeling analysis. Nomenclature used in this work is as shown in Fig. 3.

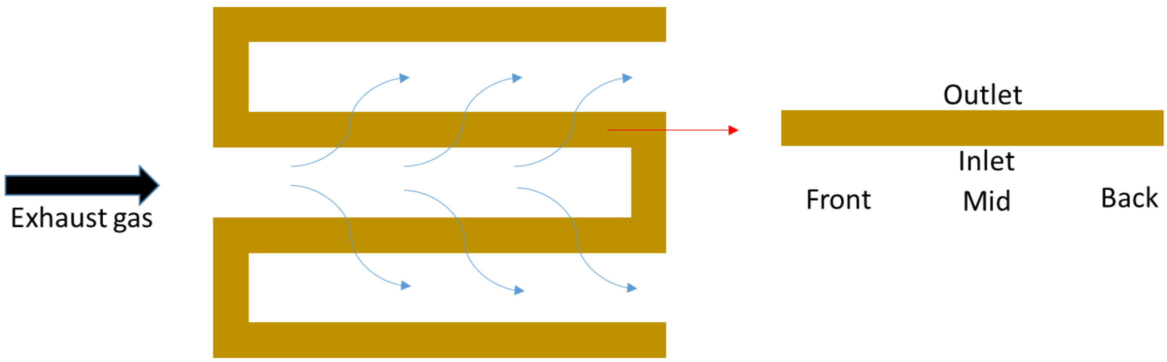

Fig. 3. Exhaust flow pathway into a GPF and nomenclature used in this work.

3. Results and discussion

3.1 Filter performance

Ash-loaded GPF samples were visually observed using a microscope as shown in Fig. 4. When ash loading was 10 g/L, slight ash coating on wall surface was observed in the back side of the filter (2^{nd} image for the ash loading of 10 g/L). Short ash plugs were partly noted on channels in the very end of the filter (3^{rd} image for the ash loading of 10 g/L). In comparison, with ash loading of 20 g/L, all the channels were filled with ash plugs in the same back of the filter (2^{nd} image for the ash loading of 20 g/L), as noted in the figure, demonstrating significant ash plug growth. This result seems to support previous work [1] that ash plugs grow after filling surface pores. However, it should be noted that since the capacity of ash loading is dependent on filter geometry and porosity, the ash plug growth rate would be different with different types of filters.

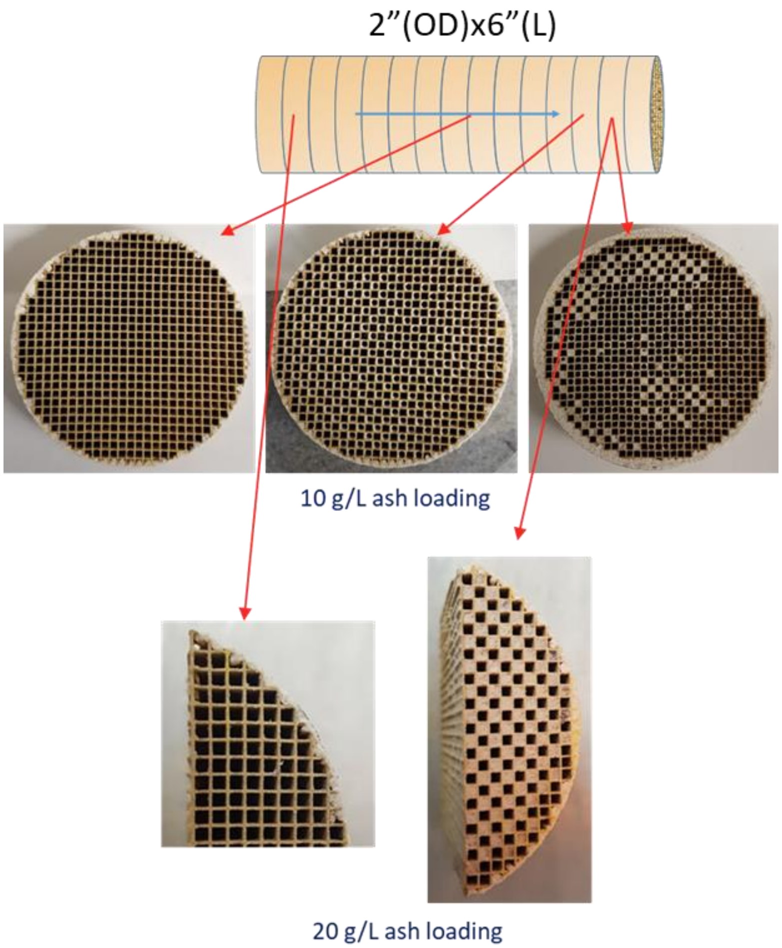

Fig. 4. Microscopic front views of sliced ash-loaded GPF samples. The three photos in the upper part are for 10 g/L ash loading and the two photos in the bottom part are for 20 g/L ash loading.

Fig. 5 shows changes in pressure drop and filtration efficiency with increased ash loading up to 10 g/L. The pressure drop increased gradually with ash loading, so the pressure drop at ash loading of 10 g/L is almost twice that at no ash loading, indicating pore pathways were greatly hindered. Although this result cannot be directly compared to others due to different experimental approaches, it is consistent with Lambert et al. that the pressure drop increased linearly with increased mileage on a vehicle [6]. While the pressure drop steadily increased with ash loading, mass and number filtration efficiencies also increased up to an ash loading of 2 g/L, then increased only slightly with further ash loading. Since the filtration tests were performed in each case just after a soot oxidation and removal step, filtration efficiencies are expected to be even higher than these results in vehicle conditions where soot is bound with ash in pores. This result confirms that a slight ash loading can block soot penetration into filters by trapping soot particles and narrowing pathways through the surface-pore level. [26, 27]. Based on the filtration efficiency and pressure drop data, it appears that the ash loading undergoes three phases: deposition of ash into surface pores (ash loading up to 2 g/L), the formation of an ash layer on the filter channel walls (ash loading of 2 – 10 g/L), and ash plug formation (ash loading > 10 g/L). However, it is uncertain whether ash penetration into pores continued during the ash cake stage.

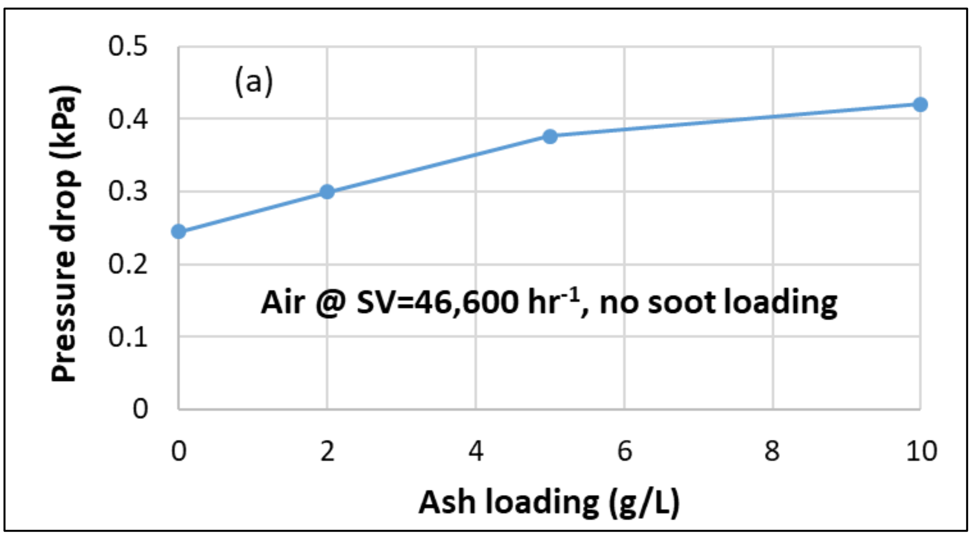

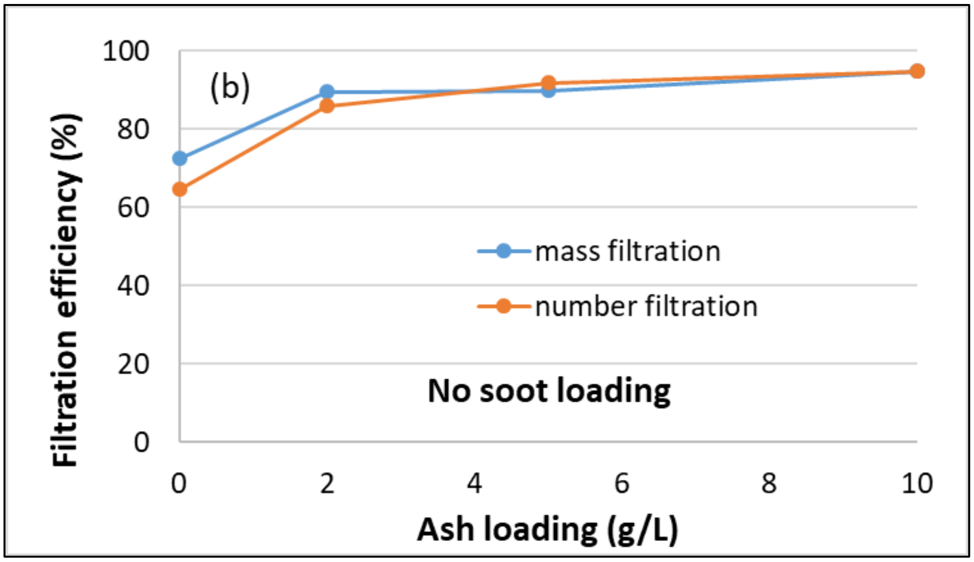

Fig. 5. (a) Pressure drop changes with ash loading, and (b) number and mass filtration efficiencies with ash loading under 1250 rpm and 25% load condition.

Fig. 6 shows 2D section views from the XRT measurements of select filter samples. The 2D images show that porosity appeared to decrease with catalyst coating and ash-loading, but the resolution is not sufficient to identify coating materials and ash from the base cordierite component. However, since the image contrast is sufficient to segment pore space from combined cordierite, catalyst and ash components, pore analysis was successfully performed.

While a thin ash layer distinct from the wall was observed for the field-aged sample, it was not noted for the lab-aged sample. The tightly-bound ash layer on the field-aged filter was retained during the sample preparation process, but loosely-bound ash on the lab-aged filter was not, despite the thick layers observed in Fig. 4. However, the gray color representing the ash layer on the field-aged filter could not be conclusively separated from the white color due to low contrast. In the following results, therefore, porosity analysis of the field-aged sample was excluded.

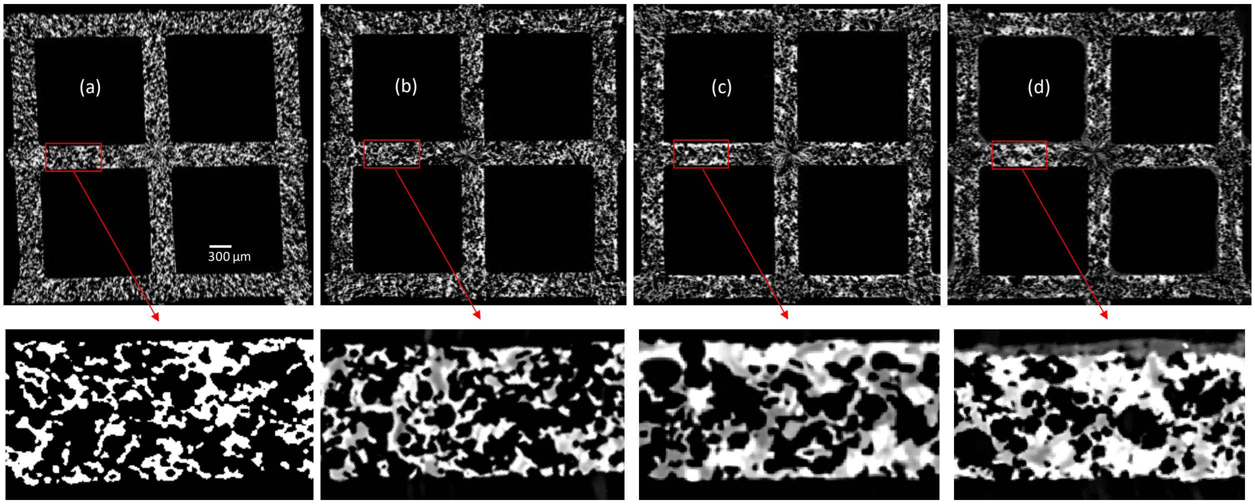

Fig. 6. 2D images of different filter samples by XRT: (a) bare filter, (b) coated filter, (c) lab-aged filter with ash loading of 20 g/L, and (d) field-aged filter with 100,000 miles. White color is the filter material which may include coating and ash materials, while black indicates pore space.

The impacts of catalyst coating and ash-loading were found to be significant for pore size distribution when number density is considered (Fig. 7a). The peak number density at a pore diameter of 60 µm did not shift irrespective of coating and ash-loading, similar to results observed by Václavík et al.[16] who examined the coating effect. With coating and ash-loading, the peak number density gradually decreased while the number of pores smaller than 20 µm increased. According to the modeling work of Gong and Rutland [28], filtration efficiency tends to decrease with large pores. They also showed that the most effective pores that achieve high filtration efficiency were obtained in the pore diameters between 10 to 30 µm. In this light, the increased filtration efficiency from ash loading is closely related with the increased population of smaller pores as ash loading lowered the peak density at 60 µm. It is interesting to note that pore size distributions were very similar for front, mid and back positions with ash loading, although locations nearer the back position tended to slightly lower peak number density. Since ash plugs were not found at the front position as shown in Fig. 4, it is surprising that the pore size distributions were comparable at different locations. Based on the number-based size distribution, volume density was further computed as noted in Fig. 7b. Because the influence of pores below 20 μm had an insignificant effect on pore volume, the overall shapes were similar, with no noticeable trend due to coating and ash-loading. The largest pores were found to be less than 200 μm.

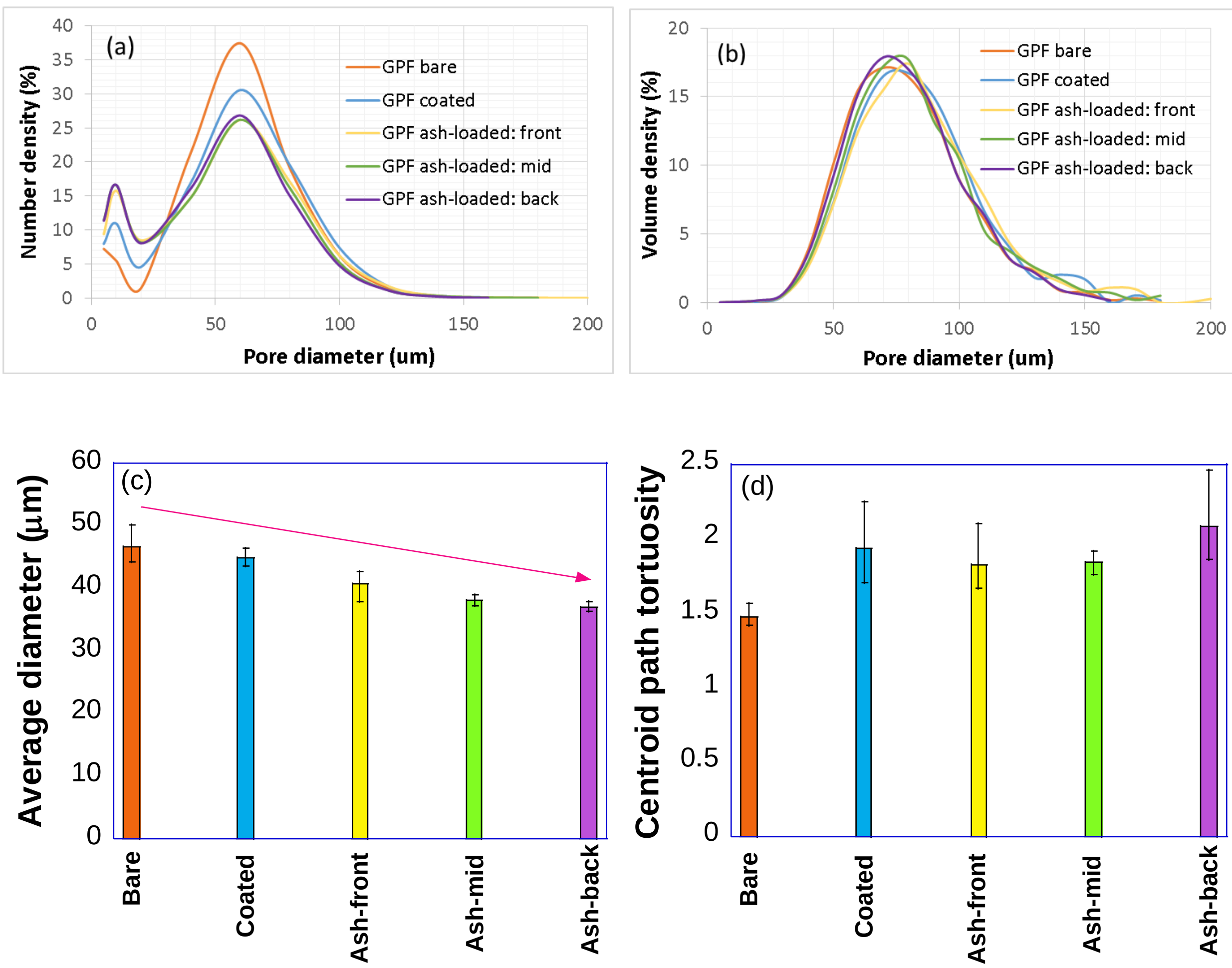

Fig. 7. Pore size distribution of the filter samples of (a) number density and (b) volume density, (c) average pore diameter, and (d) central path tortuosity. The error bars show min and max for each case.

The decrease in the peak number density with coating and ash loading was consistent with the observed decrease in average pore diameter as shown in Fig. 7c. It should be noted that some macropores and mesopores inside the coating and ash cannot be measured by the XRT [15, 16]. The bare filter has a pore diameter of around 47 μm and it decreased to 38 μm with ash loading at the back position. It should be noted that the median pore diameter of the bare and coated filters were 20.9 and 18.7 μm, respectively, from the MIP measurements, which were less than half that measured by the XRT method (Fig. 7c showed average values, which were similar to median values in this work). Although many uncounted small pores below the detection limit of 2.93 μm could be one cause of the discrepancy, another may be that MIP cannot correctly measure pore sizes when larger pores are connected to narrow throats [29]. The different pore size distributions between MIP and XRT were well noted in Václavík et al. [16]. In addition, although number-based pore size distributions appeared to be very similar regardless of ash-loaded position in Fig. 7a, average pore diameter was slightly larger at the front position, suggesting the pore plugging process was more advanced in the mid and back positions. Tortuosity measurements would explain the increased pressure drop, because a shorter flow path through the filter wall would decrease the pressure drop. However, Fig. 7d indicated that although the centroid path tortuosity of the bare filter appeared to be lower than those of coated and ash-loaded filters, the values were inconsistent for coated and ash-loaded filters. This may be because the parameter could not capture complex pore pathways. Therefore, increases in pressure drop due to catalyst coating and ash loading seem to be better represented by reduced pore sizes in these results.

Fig. 8 shows 3D images of all the closed pores separated from open pores. It is apparent that closed pore size and area significantly increased with ash loading. While closed pores appeared to be homogeneously distributed from inlet to outlet for the bare filter, they were observed to be more populated on the surface side for the ash-loaded filter. In addition, the increase in closed pores on the outlet side demonstrate that ash penetration reached this location, which was supported by observations using a DPF with ammonium sulfate particles [26]. As noted in Fig. 5b, since soot particles can still escape filters, especially at an early filtration stage, it is expected that some would be trapped inside pores up to the outlet side. As soot is oxidized during the oxidation process, ash particles would remain on pore necks. Since we did not examine porosity changes with increased ash loading, it is not clear whether ash particles could further transport to narrow pore necks.

The quantified results from Fig. 9a indicate that total porosity decreased from 63.7% to 57.6% with coating and it further decreased to below 50% for mid and back positions with ash loading. The ratio of open porosity to total porosity also decreased from 99.98% to 99.89% with coating and it further decreased below 99% for mid and back positions with ash loading. Coating and ash-loading must have occupied some space in open pores which are only accessible by coating fluid and exhaust gas. Therefore, the reduction in total porosity is directly related with decreased open porosity, which partly contributed to increased closed porosity as evident in Fig. 8. Fig. 9b also shows that closed pores were shifted to larger sizes due to coating and ash-loading. In consideration of population, therefore, increased numbers of pores below 20 μm with coating and ash-loading in Fig. 7a were probably due to increased closed pores. The increased fraction of closed pores likely contributed to increased pressure drop with ash loading, as penetration pathways were noticeably reduced.

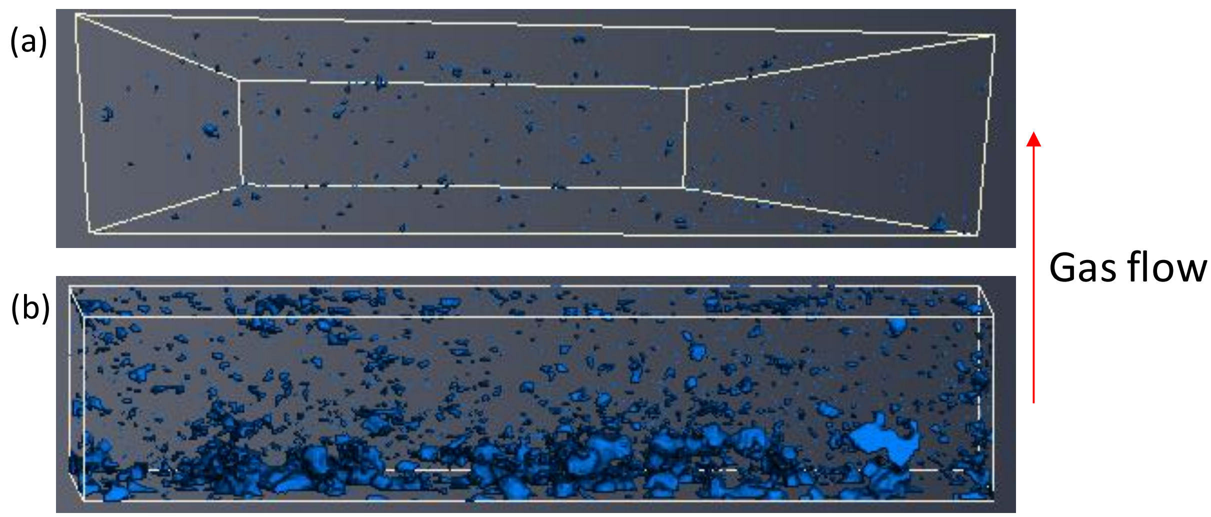

Fig. 8. 3D images of closed pores in (a) bare filter, and (b) ash-loaded back part of filter. Bottom sides indicate inlet.

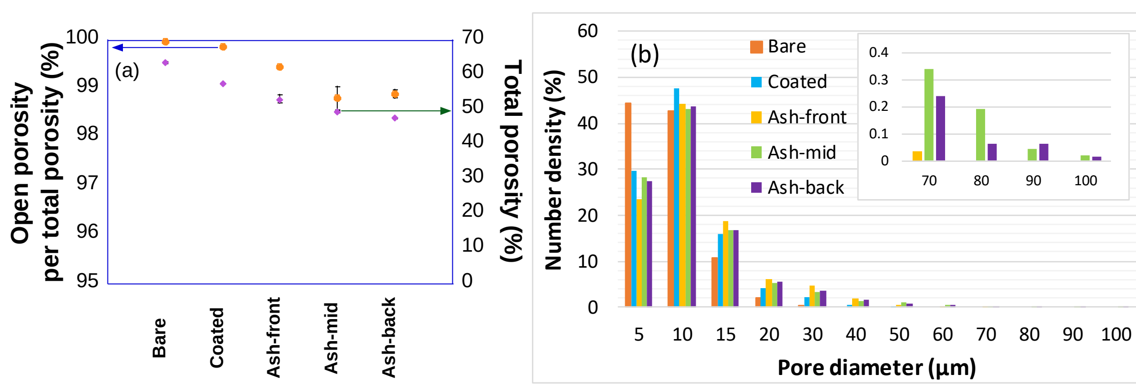

Fig. 9. Impacts of coating and ash loading on: (a) changes in open porosity and total porosity, and (b) number-based closed pore size distribution. Circles and diamonds in (a) indicate open porosity per total porosity and total porosity, respectively, where the error bars show min and max for each case.

Two-dimensional sections of the XRT data on the filters in Fig. 10 clearly show that while pore shapes and distributions were visually similar between inlet and outlet sides for the bare filter, they were found to be quite different for the ash-loaded filter. It is interesting to note that pore shapes and distributions of the outlet side of the ash-loaded filter were also comparable to those of the bare filter and the coated filter, despite coating and ash loading, implying that the impacts of coating and ash-loading on pore structure is minor in the case of outlet sides. However, the inlet side was markedly different as shown in Fig. 10c. Many appeared to be plugged with ash (though the ash portion was not distinguished from material and coating), and remaining pores appeared to be round, rather than irregular shapes like those in Figs. 10a, b and d, possibly because large pores were smoothed out as narrow pathways and sharp features were first to be filled with ash particles.

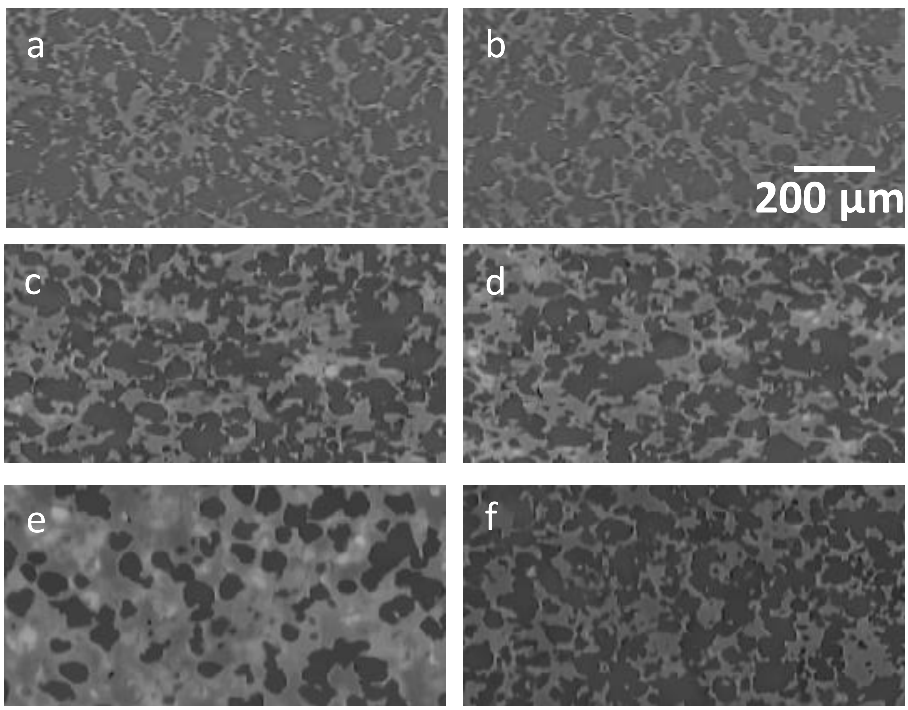

Fig. 10. 2D images of filters: (a) inlet side of the bare filter, (b) outlet side of the bare filter, (c) inlet side of the coated filter, (d) outlet side of the coated filter, (e) inlet side of the ash-loaded outside filter, and (f) outlet side of the ash-loaded outside filter.

Porosity changes in 2D images were measured by areal porosity along the direction of gas flow as shown in Fig. 11. Although the porosity was slightly reduced at the outermostinlet and outlet sides, it was similar for the bare and coated filters, indicating that the pore distribution was homogeneous. This trend is different from what others have observed, showing higher porosity near the wall surfaces [10, 26]. It should be noted that while they measured the porosity distribution from 1D slices using 2D images, we did the work from 2D slices using 3D images. Also, since pores located at the outermost inlet and outlet surfaces are not distinguished from the outside space despite axis alignment, several outermost surface slices which did not show clear pore/material boundaries were excluded in the analysis. With ash-loading, by comparison, the porosity experienced steep decreases at small filter depth, and it gradually increased up to the level of the coated filter, which suggests that ash particles penetrated deeply into the wall, rather than just the surface pore level. The front of the ash-loaded filter had larger porosity at small filter depth than did the mid and back, supporting inhomogeneous ash plugging at different locations in the filters.

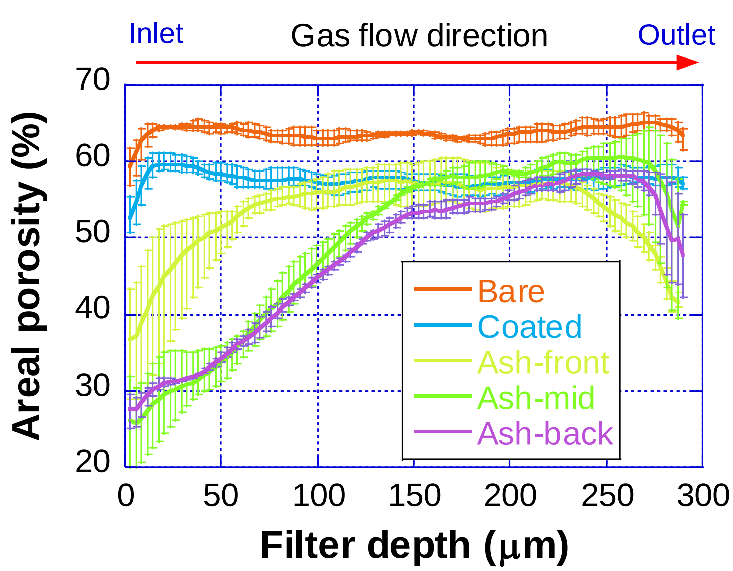

Fig. 11. Areal porosity changes along the direction of gas flow.

These results suggest that ash particles are embedded many tens of microns into the filter wall. This would give the high-porosity GPF a large capacity to contain ash within inside wall, not limited to the surface pore level. This is in contrast to some other work in the literature. According to Sanui and Hanamura [27], particulate matter penetration deeper than the surface pore level was rarely observed because of obstructed gas passages. Although the average PM penetration depth would be dependent on porosity and pore structure, they observed it to be approximately 20 µm when SiC of 42% porosity was used. Direct observations of a full useful life (FUL, 150000 mi) filter showed ash penetration to be approximately 60 µm after cross section ion milling was performed, with only surface-level ash penetration indicated [6]. These differences may be due to different operating conditions such as PM filtration, filter regeneration, exhaust gas flow rate and filter geometry. In addition to possible damage of weakly-bound ash particles during the machining process, 2D microscopic analysis from cross-cut images may lead to misinterpretation as ash distribution is inhomogeneous as shown in Fig. 12.

Although the XRT analysis cannot identify ash components from filter material, this non-destructive method gives powerful information of ash distribution in 3D images from high-resolution pore analysis as noted in this work. A preliminary exploration of a non-destructive method using 3D elemental analysis from x-ray fluorescence spectroscopy (XRF) tomography is presented in Li et al. to better answer ash distribution in a GPF [30]. Though advancements in sample size are needed, it will be able to provide valuable insights into ash behaviors in DPF and GPF with aging.

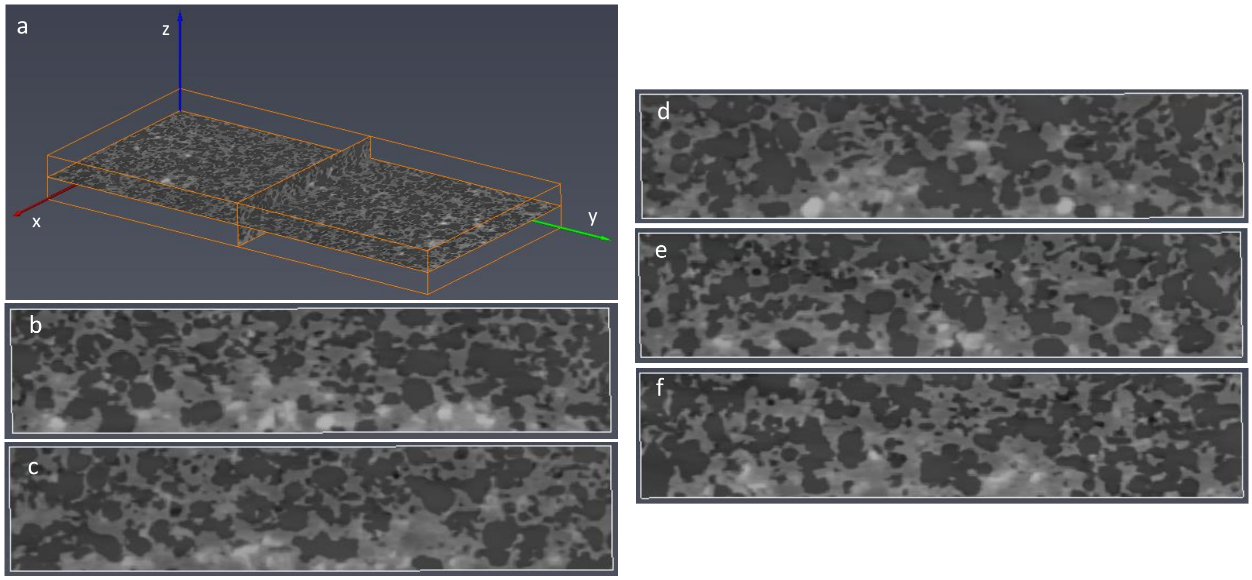

Fig. 12. Images of the back position of the ash-loaded filter: (a) 2D cross-cut images with xy and xz planes in a box of the examined wall, (b) 1st 2D cross-cut image among 1001 slides along the y-axis, (c) 250th 2D cross-cut image among 1001 slides along the y-axis, (d) 500th 2D cross-cut image among 1001 slides along the y-axis, (e) 750th 2D cross-cut image among 1001 slides along the y-axis, and (f) 1001th 2D cross-cut image among 1001 slides along the y-axis.

4. Conclusions

XRT was employed to explore changes in pore structure from a bare GPF, catalyst-coated GPF and the front, mid, and back positions of an ash-loaded GPF to better understand the impacts of coating and ash-loading. The examination of 3D images showed consistent trends with coating and ash-loading: The number of pores at the peak in the size distribution (60 µm) gradually decreased with coating and ash-loading while the number below 20 µm increased; average pore diameter, total porosity and closed porosity were observed to decrease. 3D visualization clearly indicated that closed pores which were homogeneously distributed in the bare filter became more populated on the wall surface with ash-loading. Also, closed pores which were found only below 30 µm for the bare filter expanded toward 50 and 100 µm with coating and ash-loading, respectively. Analyses of 2D areal porosity from inlet to outlet in the direction of gas flow indicated that most ash particles were contained up to approximately 150 µm, which was much deeper than 2D cross-cut microscopic analyses from the literature and our observations, which require destructive machining steps with limited local access. In conclusion, increased pressure drops from coating and ash-loading were attributed to an increase in pore blocking which greatly removed flow pathways throughout the porous filters.

Conflicts of Interest: There exist no conflicts of interest.

ACKNOWLEDGMENT

The authors thank the Advanced Engine Combustion Program at the U.S. Department of Energy Office of Vehicle Technologies for sponsorship of this work. Also, the authors are grateful to Dr. Jimmie Williams from Corning Inc. for MIP results and to Drs. Jinwoo Choung and Chibum In from Hyundai Motor Company for valuable discussions. The XRT measurements were performed at the 7BM beamline at the Advanced Photon Source (APS). The APS is supported by the U. S. Department of Energy, Office of Science, under contract No. DE-AC02-06CH11357.

REFERENCES

1. Sappok A, Wong VW (2010) Lubricant-Derived Ash Properties and Their Effects on Diesel Particulate Filter Pressure-Drop Performance. J Eng Gas Turbines Power 133:032805-032805–12 . doi: 10.1115/1.4001944

2. Guan B, Zhan R, Lin H, Huang Z (2015) Review of the state-of-the-art of exhaust particulate filter technology in internal combustion engines. J Environ Manage 154:225–258 . doi: 10.1016/j.jenvman.2015.02.027

3. Lambert C, Chanko T, Dobson D, Liu X, Pakko J (2017) Gasoline Particle Filter Development. Emiss Control Sci Technol 3:105–111 . doi: 10.1007/s40825-016-0055-x

4. Custer N, Kamp CJ, Sappok A, Pakko J, Lambert C, Boerensen C, Wong V (2016) Lubricant-Derived Ash Impact on Gasoline Particulate Filter Performance. SAE Int J Engines 9:1604–1614 . doi: 10.4271/2016-01-0942

5. Shao H, Lam W, Remias J, Roos J, Choi S, Seong H (2016) Effect of Lubricant Oil Properties on the Performance of Gasoline Particulate Filter (GPF). SAE Int J Fuels Lubr 9:650–658 . doi: 10.4271/2016-01-2287

6. Lambert CK, Bumbaroska M, Dobson D, Hangas J, Pakko J, Tennison P (2016) Analysis of High Mileage Gasoline Exhaust Particle Filters. SAE Int J Engines 9:1296–1304 . doi: 10.4271/2016-01-0941

7. Liu Y, Su C, Clerc J, Harinath A, Rogoski L (2015) Experimental and Modeling Study of Ash Impact on DPF Backpressure and Regeneration Behaviors. SAE Int J Engines 8: . doi: 10.4271/2015-01-1063

8. Yang J, Stewart M, Maupin G, Herling D, Zelenyuk A (2009) Single wall diesel particulate filter (DPF) filtration efficiency studies using laboratory generated particles. Chem Eng Sci 64:1625–1634 . doi: 10.1016/j.ces.2008.12.011

9. Hayashi H, Kubo S (2008) Computer simulation study on filtration of soot particles in diesel particulate filter. Comput Math Appl 55:1450–1460 . doi: 10.1016/j.camwa.2007.08.012

10. Gong J, Stewart ML, Zelenyuk A, Strzelec A, Viswanathan S, Rothamer DA, Foster DE, Rutland CJ (2018) Importance of filter's microstructure in dynamic filtration modeling of gasoline particulate filters (GPFs): Inhomogeneous porosity and pore size distribution. Chem Eng J 338:15–26 . doi: 10.1016/j.cej.2018.01.006

11. Gong J, Viswanathan S, Rothamer DA, Foster DE, Rutland CJ (2017) Dynamic Heterogeneous Multiscale Filtration Model: Probing Micro- and Macroscopic Filtration Characteristics of Gasoline Particulate Filters. Environ Sci Technol 51:11196–11204 . doi: 10.1021/acs.est.7b02535

12. Anovitz LM, Cole DR (2015) Characterization and Analysis of Porosity and Pore Structures. Rev Mineral Geochem 80:61–164 . doi: 10.2138/rmg.2015.80.04

13. Gaboreau S, Robinet J-C, Prêt D (2016) Optimization of pore-network characterization of a compacted clay material by TEM and FIB/SEM imaging. Microporous Mesoporous Mater 224:116–128 . doi: 10.1016/j.micromeso.2015.11.035

14. Yamamoto K, Sakai T (2016) Effect of Pore Structure on Soot Deposition in Diesel Particulate Filter. Computation 4:46 . doi: 10.3390/computation4040046

15. Kočí P, Isoz M, Plachá M, Arvajová A, Václavík M, Svoboda M, Price E, Novák V, Thompsett D (2017) 3D reconstruction and pore-scale modeling of coated catalytic filters for automotive exhaust gas aftertreatment. Catal Today. doi: 10.1016/j.cattod.2017.12.025

16. Václavík M, Plachá M, Kočí P, Svoboda M, Hotchkiss T, Novák V, Thompsett D (2017) Structure characterisation of catalytic particulate filters for automotive exhaust gas aftertreatment. Mater Charact 134:311–318 . doi: 10.1016/j.matchar.2017.11.011

17. Chen Z, Wang X, Giuliani F, Atkinson A (2015) Analyses of microstructural and elastic properties of porous SOFC cathodes based on focused ion beam tomography. J Power Sources 273:486–494 . doi: 10.1016/j.jpowsour.2014.09.131

18. Boever ED, Varloteaux C, Nader FH, Foubert A, Békri S, Youssef S, Rosenberg E (2012) Quantification and Prediction of the 3D Pore Network Evolution in Carbonate Reservoir Rocks. Oil Gas Sci Technol – Rev D'IFP Energ Nouv 67:161–178 . doi: 10.2516/ogst/2011170

19. Hemes S, Desbois G, Urai JL, Schröppel B, Schwarz J-O (2015) Multi-scale characterization of porosity in Boom Clay (HADES-level, Mol, Belgium) using a combination of X-ray μ-CT, 2D BIB-SEM and FIB-SEM tomography. Microporous Mesoporous Mater Complete:1–20 . doi: 10.1016/j.micromeso.2015.01.022

20. Manickam SS, Gelb J, McCutcheon JR (2014) Pore structure characterization of asymmetric membranes: Non-destructive characterization of porosity and tortuosity. J Membr Sci 454:549–554 . doi: 10.1016/j.memsci.2013.11.044

21. Peng S, Hu Q, Dultz S, Zhang M (2012) Using X-ray computed tomography in pore structure characterization for a Berea sandstone: Resolution effect. J Hydrol 472–473:254–261 . doi: 10.1016/j.jhydrol.2012.09.034

22. Ou X, Zhang X, Lowe T, Blanc R, Rad MN, Wang Y, Batail N, Pham C, Shokri N, Garforth AA, Withers PJ, Fan X (2017) X-ray micro computed tomography characterization of cellular SiC foams for their applications in chemical engineering. Mater Charact 123:20–28 . doi: 10.1016/j.matchar.2016.11.013

23. Kastengren A, Powell CF, Arms D, Dufresne EM, Gibson H, Wang J (2012) The 7BM beamline at the APS: a facility for time-resolved fluid dynamics measurements. J Synchrotron Radiat 19:654–657 . doi: 10.1107/S0909049512016883

24. Matusik KE, Duke DJ, Kastengren AL, Sovis N, Swantek AB, Powell CF (2017) High-resolution X-ray tomography of engine combustion network diesel injectors. Int J Engine Res 1468087417736985 . doi: 10.1177/1468087417736985

25. Gürsoy D, De Carlo F, Xiao X, Jacobsen C (2014) TomoPy: a framework for the analysis of synchrotron tomographic data. J Synchrotron Radiat 21:1188–1193 . doi: 10.1107/S1600577514013939

26. Karin P, Cui L, Rubio P, Tsuruta T, Hanamura K (2009) Microscopic Visualization of PM Trapping and Regeneration in Micro-Structural Pores of a DPF Wall. SAE Int J Fuels Lubr 2:661–669 . doi: 10.4271/2009-01-1476

27. Sanui R, Hanamura K (2016) Electron microscopic time-lapse visualization of surface pore filtration on particulate matter trapping process. J Microsc 263:250–259 . doi: 10.1111/jmi.12386

28. Gong J, Rutland CJ (2015) PDF-Based Heterogeneous Multiscale Filtration Model. Environ Sci Technol 49:4963–4970 . doi: 10.1021/acs.est.5b00329

29. Giesche H (2006) Mercury Porosimetry: A General (Practical) Overview. Part Part Syst Charact 23:9–19 . doi: 10.1002/ppsc.200601009

30. Li L, Choi S, Seong HJ, Vogt S X-ray Fluorescence Microscopy analyses of Three-Way Catalyst aging and deactivation in Gasoline Particulate Filter Application, 2016 Microscopy & Microanalysis, July 24 - 28, Columbus (Ohio, USA), 2016.